Chemical Science

ROYAL SOCIETY OF CHEMISTRY

EDGE ARTICLE

View Article Online
View Journal | View Issue

Cite this: *Chem. Sci.*, 2022, **13**, 5650

All publication charges for this article have been paid for by the Royal Society of Chemistry

Zwitterionic iodonium species afford halogen bond-based porous organic frameworks†

Natalia S. Soldatova, [a] Pavel S. Postnikov, *[ab] Daniil M. Ivanov,[ac] Oleg V. Semyonov,[a] Olga S. Kukurina,[a] Olga Guselnikova, [ad] Yusuke Yamauchi, [de] Thomas Wirth, [f] Viktor V. Zhdankin, [g] Mekhman S. Yusubov,[a] Rosa M. Gomila, [h] Antonio Frontera, [i] Giuseppe Resnati *[aj] and Vadim Yu. Kukushkin *[c]

Porous architectures characterized by parallel channels arranged in honeycomb or rectangular patterns are identified in two polymorphic crystals of a zwitterionic 4-(aryliodonio)-benzenesulfonate. The channels are filled with disordered water molecules which can be reversibly removed on heating. Consistent with the remarkable strength and directionality of the halogen bonds (XBs) driving the crystal packing formation, the porous structure is stable and fully preserved on almost quantitative removal and readsorption of water. The porous systems described here are the first reported cases of one-component 3D organic frameworks whose assembly is driven by XB only (XOFs). These systems are a proof of concept for the ability of zwitterionic aryliodonium tectons in affording robust one-component 3D XOFs. The high directionality and strength of the XBs formed by these zwitterions and the geometrical constraints resulting from the tendency of their hypervalent iodine atoms to act as bidentate XB donors might be key factors in determining this ability.

Received 11th February 2022
Accepted 30th March 2022

DOI: 10.1039/d2sc00892k

rsc.li/chemical-science

Introduction

Metal organic frameworks (MOFs) and covalent organic frameworks (COFs) play a significant role in science and technology. Such systems are widely applied in gas storage and separation,[1–7] capture of hazardous compounds (*e.g.*, heavy metals, pesticides, and volatile organic compounds),[8–12] catalysis,[13–17] *etc.* The approaches for the preparation of these systems include the interaction between structurally defined building blocks with the formation of coordination (MOFs) or covalent (COFs) bonds.

Very recently, the modern palette of porous materials has been enriched by novel systems wherein the structural units are assembled *via* relatively weak interactions, with supramolecular organic frameworks[18–20] (SOFs) and hydrogen-bonded organic frameworks[21–26] (HOFs) being the most common representatives. However, the development of these materials is challenging as a consequence of the lower directionality of weak noncovalent bonds in comparison to coordination or covalent bonds affording MOFs and COFs.[27,28] In this context, halogen bonding (XB) is becoming a novel tool for the controlled assembly of molecular tectons into highly ordered frameworks[29,30] and is here employed for the obtainment of 3D and *one-component* purely halogen-bonded organic frameworks (XOFs). It was considered that the high directionality of the interaction might act as an advantage of the approach. Notably, a one-component 2D XOF was observed in crystals of tetrabromobenzene-1,4-dicarboxylic acid.[30]

Among the wealth of porous molecular crystals wherein XB contributes to sustaining the architecture, only two examples that can be considered as 3D XOFs were obtained *via* (i) cocrystallization of the tetrahedral pyridine-based XB acceptor and 1,3,4,5-tetraiododifluorobenzene to form a *di-component* XOF[29] and (ii) assembly of a heterotopic tecton to give an *unstable* 3D XOF.[31]

[a]*Research School of Chemistry and Applied Biomedical Sciences, Tomsk Polytechnic University, Tomsk 634034, Russian Federation. E-mail: postnikov@tpu.ru*

[b]*Department of Solid State Engineering, Institute of Chemical Technology, Prague 16628, Czech Republic*

[c]*Institute of Chemistry, Saint Petersburg State University, Saint Petersburg 199034, Russian Federation. E-mail: v.kukushkin@spbu.ru*

[d]*JST-ERATO Yamauchi Materials Space-Tectonics Project, National Institute for Materials Science (NIMS), 1-1 Namiki, Tsukuba, Ibaraki 305-0044, Japan*

[e]*Australian Institute for Bioengineering and Nanotechnology (AIBN), The University of Queensland, Brisbane, QLD 4072, Australia*

[f]*School of Chemistry, Cardiff University, Park Place, Cardiff, UK*

[g]*Department of Chemistry and Biochemistry, University of Minnesota, Duluth, MN 55812, USA*

[h]*Serveis Científico-Tècnics, Universitat de les Illes Balears, Crta. de Valldemossa Km 7.5, 07122 Palma de Mallorca, Spain*

[i]*Departament de Química, Universitat de les Illes Balears, Crta. de Valldemossa Km 7.5, 07122 Palma de Mallorca, Spain*

[j]*NFMLab, Department of Chemistry, Materials and Chemical Engineering "Giulio Natta"; Politecnico di Milano, via Mancinelli 7, I-20131 Milano, Italy. E-mail: giuseppe.resnati@polimi.it*

† Electronic supplementary information (ESI) available. CCDC 2096180, 2096183, 2096184 and 2096193. For ESI and crystallographic data in CIF or other electronic format see https://doi.org/10.1039/d2sc00892k

The well-developed strategy of assembly of XB donors with nitrogen-based XB acceptors furnishes,[32,33] in particular, halogen-bonded 3D structures (exhibiting diamondoid-like cage entities), which are promising porous materials; these structures have not been tested as adsorbents.[34–38] In some other cases, assembly of iodine species with N-based XB acceptors provided 2D or 1D architectures, featuring cavities.[29,39–41]

Other reported examples of XB-assembled SOFs are built by the simultaneous action of XB and hydrogen bonding (HB).[42,43]

Diaryliodonium salts[44,45] can function as useful building blocks in supramolecular chemistry[46] due to their ability to form discrete adducts and 1D chains or ribbons.[47–50] The iodine typically functions as a bidentate XB donor[51–56] and the XB acceptor is, by far in most cases, the anion. Despite the wide applicability of iodonium salts as halogen bond donors in catalysis,[54–57] the formation of 3D structures with well-defined pores is still unknown. Among other iodonium salts, the zwitterionic compounds can be promising for the directed design of 3D networks due to the presence of two binding sites. Nevertheless, the number of zwitterionic systems characterized *via* single-crystal X-ray diffractometry (XRD) is too small to enable statistically meaningful statements, but it is interesting to observe that although 1D chains and ribbons[58–62] are the most common halogen-bonded systems formed by these iodonium salts, the tendency to form multidimensional nets, *e.g.*, 2D[59,63] networks, seems definitely higher than when starting from diaryliodonium salts wherein the positive and negative sites are in different molecular entities.

We decided to verify whether zwitterionic iodonium species can indeed function as promising tectons for the reliable design and synthesis of multidimensional supramolecular architectures in general and new XOFs in particular. In this study, we synthesized novel zwitterionic 4-(aryliodonio)benzene-sulfonate species (Scheme 1) and we report that crystallization of one of them leads to porous XOFs. We reasoned that the strong electrostatic attraction between the cationic and anionic sites in the zwitterion may act synergistically with the remarkable directionality of the XB and enable the self-assembly of robust XOFs. The design and preparation of XOFs based on zwitterionic iodonium salts may thus represent a new opportunity in the challenging and rewarding field of novel porous organic materials. Density functional theory (DFT) calculations provide an insight into the relative intensity of both σ-holes located at the extensions of both C–I bonds and the energetic features associated with the XBs.

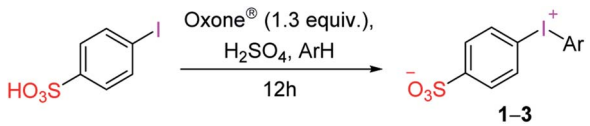

Scheme 1 Synthesis of zwitterionic iodonium salts **1** (Ar = 2,4,6-$Me_3C_6H_2$; 74%), **2** (2,5-$Me_2C_6H_3$; 60%), and **3** (4-ClC_6H_4; 98%).

Results and discussion

Halogen bonding and crystal packing in 4-(aryliodonio)-benzenesulfonates

4-Iodobenzenesulfonic acid was used as the starting material for preparing zwitterionic tectons for obtaining XOFs. Iodonium salts **1–3** were synthesized oxidizing this compound with Oxone®/H_2SO_4 (ref. 49 and 64–68) and coupling it with mesitylene, 1,4-dimethylbenzene, and chlorobenzene (Scheme 1 and Section S1†). On crystallization of **1** from MeOH : H_2O mixtures, two different crystal forms **1a** and **1b** were obtained depending on the water content: 15 : 1 (v/v) afforded **1a**, while methanol with >20% H_2O afforded **1b**. This behavior indicates that for this iodonium species the solvent plays an active role, possibly a templating role, in the crystal construction. Notably, the structures of **2** and **3** exhibit similar 1D-patterns to those in **1b**, but only **1b** features the porous structure (see later).

The overall crystal packings of iodonium derivatives **1–3** are quite different from each other, but strict similarities exist in the attractive interactions driving zwitterion binding. Some C–H···π and C–H···O HBs are present in crystals **1–3** but the overall crystal packing of these systems is controlled by the short, directional, and charge assisted I···O XBs (Table 1). Iodine atoms function as bidentate XB donors and sulfonate moieties as bidentate acceptors, with two out of the three sulfonate O atoms acting as monodentate donors of electron density. As typical for XBs, oxygen atoms approach iodine atoms approximately on the extension of C–I covalent bonds. C–I···O angles span the range 167–175° but in two interactions involving the disordered sulfonated group in **1b** where greater deviations from linearity are observed.

The I···O distances, typically varying in the range 2.73–3.05 Å, are similar to those in crystalline 2-(aryliodonio)benzene-sulfonates[60] and are substantially shorter than the sum of Bondi vdW radii[69] (Σ_{vdW}(O + I) is 3.5 Å). Deviations from these most common values are observed once again for interactions involving the disordered sulfonate group in **1b**, the I···O1 and I···O3D distances increasing to 3.231 and 3.267 Å. Interestingly, in **1b**, **2**, and **3**, the C–I···O XBs opposite the phenylsulfonyl moiety are 0.1–0.2 Å longer than the C–I···O XBs opposite the other aryl group at iodine, despite the σ-holes opposite the former moiety being more positive than those opposite the second one. A possible rationalization is suggested by the modelling of the interactional landscape present in the packings and is discussed later on. In **1a**, the difference between the two C–I···O separations is negligible and within 3σ.

A halogen-bonded dimer formed on antiparallel pairing of two zwitterions is a common motif present in all crystals **1–3**. A similar motif is present also in the zwitterion 4-($CF_3SO_2NSO_2$)C_6H_4IPh.[59] These dimers are further connected to each other *via* XBs and linear ribbons (1D-network) are present in **1b**, **2**, and **3** (Fig. 1c and S1†). To the best of our knowledge, a similar 1D-net has never been reported for any other zwitterionic iodonium salts.[59–61] One ribbon is found in the lattice of **2**, while two distinct but very similar ribbons are present in **1b** and **3**. In **1a**, any dimer formed on antiparallel pairing of two zwitterions is

Table 1 Selected geometric parameters of XBs in crystals of 4-(aryliodonio)benzenesulfonates **1–3**

Compound	C1–I⋯O	d(I⋯O), Å	∠C1–I⋯O, °	C7–I⋯O	d(I⋯O), Å	∠C7–I⋯O, °
1a	C1–I1⋯O3	2.861(4)	168.39(10)	C7–I1⋯O2	2.877(2)	170.31(10)
1b[a] chain 1	C1–I1⋯O3D	3.267(3)	166.70(8)	C7–I1⋯O1B	2.8305(16)	171.08(7)
	C1B–I1B⋯O3B	3.0577(18)	169.14(7)	C7B–I1B⋯O1D	2.755(3)	155.97(10)
1b chain 2	C1A–I1A⋯O2A	2.949(2)	173.56(9)	C7A–I1A⋯O1A	2.8173(19)	169.60(6)
2	C1–I1⋯O2	3.007(5)	171.34(17)	C7–I1⋯O1	2.864(4)	169.41(12)
3 chain 1	C1–I1⋯O3	2.900(4)	175.07(16)	C7–I1⋯O1	2.734(4)	171.94(16)
3 chain 2	C1A–I1A⋯O3A	2.910(4)	171.90(16)	C7A–I1A⋯O1A	2.763(4)	173.24(15)

[a] Probably due to rotation of one sulfonate group of chain 1 around the C–S covalent bond, the oxygen atoms of the corresponding sulfonate group are disordered and have been modeled over two positions; geometric parameters of the XBs associated with the second position are C1–I1⋯O3, d(I⋯O) 2.988(3) Å, ∠C1–I1⋯O3 171.39(7)°; C7B–I1B⋯O1, d(I⋯O) 3.231(3) Å, C7B–I1B⋯O1 149.22(9)°.

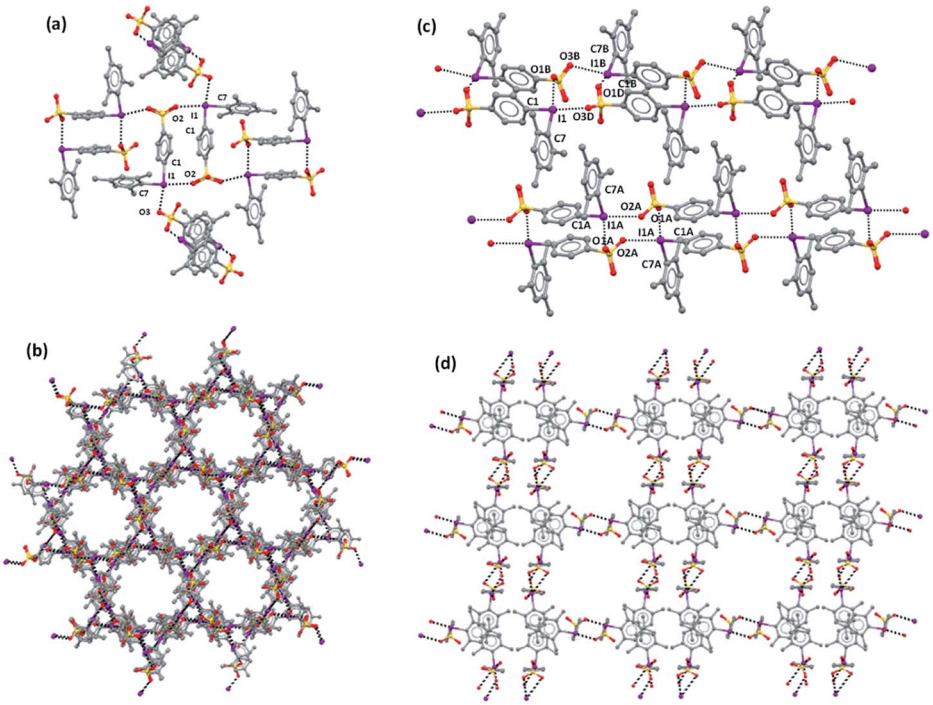

Fig. 1 Partial representation (Mercury 4.3.1, ball and stick) of the crystal packing of **1a**: (a) a halogen-bonded dimeric unit with the four appended dimeric units; (b) a view of the lattice down the *c*-axis evidencing the honeycomb-like porous structure resulting in a hexagonal channels pattern. (c) Crystal packing of **1b** showing the two ribbons (only one of the disordered sulfonate groups is depicted); (d) the rectangular pattern viewed along the *a* axis which corresponds to an analogous channel array. Hydrogen atoms are omitted; XBs are shown as dashed black lines. Color coding: grey, carbon; red, oxygen; ocher, sulfur; violet, iodine.

halogen-bonded to four other analogous dimers (Fig. 1a) and a 3D network is formed.

Consistent with the fact that the density of **2** and **3** (1.942 and 2.061 g cm^{-3}, respectively) is much greater than that of **1a** and **1b** (1.492 and 1.399 g cm^{-3}, respectively), the crystal packings of the former two systems present no voids while the packings of the latter two systems are porous and show parallel channels, along the *c* and *a* axes, respectively (Fig. 2). Water is present in these channels but could not be identified through crystallography due to its mobility.

Channels in both crystals have a cylindrical shape with a diameter of ∼10 Å in **1a** and ∼12 Å in **1b**; the percentage of empty volume is 22.5 in **1a** and 25.0 in **1b**. Before SQUEEZE in Platon[70] was applied, we identified numerous residual peaks, ranging from 1.01 to 2.70 e, in the channel structure of **1a**. We believe that the observed residual peaks are related to adsorbed disordered water that was also identified by FTIR and NMR spectroscopy; the NMR spectra of **1a** do not exhibit any signals of MeOH. Additional evidence favoring the presence of water was obtained from the IR spectra, where the water peaks were found at 3420 cm^{-1} (Fig. 3e). Moreover, NMR experiments (residual DMSO in DMSO-d_6 was used as an internal standard) clearly demonstrated a lower water content in a dried sample in comparison with the pristine sample and a sample after water adsorption (Fig. S3, ESI†).

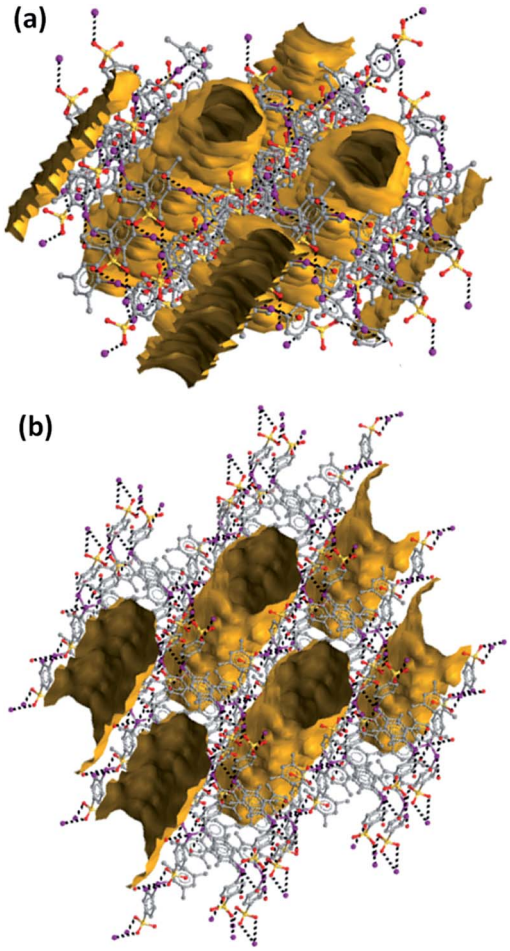

Fig. 2 Partial representation (Mercury 4.3.1, ball and stick) of the crystal packing of **1a** (a) and **1b** (b) after orientations evidencing the cylindrical shape and the parallel arrangement of the channels (contact surfaces in ocher). A probe radius of 1.2 Å and an approximate grid spacing of 0.7 Å were used to generated channels. Hydrogen atoms are omitted; XBs are dashed black lines. Color coding: grey, carbon; red, oxygen; ocher, sulfur; violet, iodine.

Parallel 1D-channels filled with solvent molecules and similar to those found in **1a** and **1b** have been observed in systems formed on assembly of pyridine based XB acceptors with 1,4-diiodoperfluorobenzene and 1,3,5-triiodoperfluorobenzene.[24,52] In **1a**, the overall arrangement of the 3D-net adopts a honeycomb-like structure (Fig. 1b) and channels display a hexagonal pattern, while in **1b** the 1D-nets assemble in a rectangular geometry (Fig. 1d) which translates into a channel array with analogous topology. In contrast to **1a**, the XRD pattern of **1b** does not agree with the simulated pattern because of the decomposition occurring on drying (Fig. S2†).

Porosity of the XOF and reversible solvent adsorption/desorption

The results of XRD stimulated us to further investigate the porosity of XOF **1a**. We started by assessing the scalability of the preparation (up to 500 mg) of this porous crystal phase. Gram quantities of the XOF were obtained and all batches showed uniform-shaped crystals, as confirmed by powder XRD and SEM images (Fig. 3b and f).

Key features for the further harnessing of XOF **1a** are its thermal stability and the possibility to remove the solvent while preserving the original crystal structure. The TG/DSC analysis revealed that crystals were stable up to 180 °C, then exothermic decomposition occurred (Fig. 3d). According to the TG data, the prepared XOF **1a** can be activated at least at 140 °C without either destruction or phase transition. The initial weight-loss is tentatively associated with the removal of solvent from the voids. To assess the crystal structure preservation on solvent removal, the crystalline powder of **1a** was dried for 1.5 hours until the weight of the sample remained constant. The powder XRD study of this batch (Fig. 3b) showed a pattern very similar to that of the pristine material, indicating the original crystal structure.

To verify the functional potential of XOF **1a**, we tested the reversibility of water adsorption/desorption from the vapor phase. The weighed sample of dried **1a** was placed in a desiccator saturated with water vapor and the weight was monitored. The amount of chemisorbed water was 5.69 mass% (calculated with respect to the mass of the pristine sample of **1a**) and this value agrees well with the mass-loss from the pristine powder (5.85 mass%) and mass-loss TG data (Fig. 3d).

The consequence of water adsorption and desorption by crystals of **1a** is fully reversible (Fig. 3a). Thus, we conducted a gravimetric determination of the adsorption capacity, along with XRD and spectroscopic monitoring, and found that the structure of **1a** is fully preserved after at least 5 cycles of adsorption followed by desorption performed on drying. These experiments indicate that XB stabilizes the XOF crystal structure that is preserved even under relatively harsh conditions of the repeated adsorption and desorption cycles.

We also performed an experiment with the adsorption of D_2O (instead of H_2O) by the dehydrated sample. The IR-spectra (Fig. 3e) revealed the appearance of $\nu_{as,s}(D_2O)$ stretching at approximately 2530 cm^{-1} and these data additionally proved the adsorption of D_2O from the gas phase by XOF **1a** (the assignment of the IR bands is provided in ESI Table S2†).

To get additional data illustrating the stability of XOF **1a**, we also carried out variable-temperature Raman spectroscopy experiments. We observed that these spectra remain unchanged even after heating XOF **1a** at 140 °C for 1 h (Fig. 3c). The Raman spectrum of **1a**, after 5 cycles of water adsorption–desorption, demonstrated the preservation of the crystal structure.

The porous structure of **1a** was also studied using nitrogen adsorption–desorption isotherm measurements. Fig. 4a shows a gradual adsorption of nitrogen gas with a small hysteresis loop. The BET surface area of the XOF exhibits an expectedly low value of 17.7 $m^2\ g^{-1}$, probably because of the presence of water in the pores. In view of the known difficulties of the Barrett–Joyner–Halenda (BJH) method,[71] the pore size distribution curve was obtained by the more accurate Non-Local Density Functional Theory (NLDFT) approach (Fig. 4b). We found that the microporous structure is indeed formed and its total pore volume is 0.017 $cm^3\ g^{-1}$. Fig. 4b shows largest pore size of about 7 Å, which corresponds to a cylindrical shaped pore with

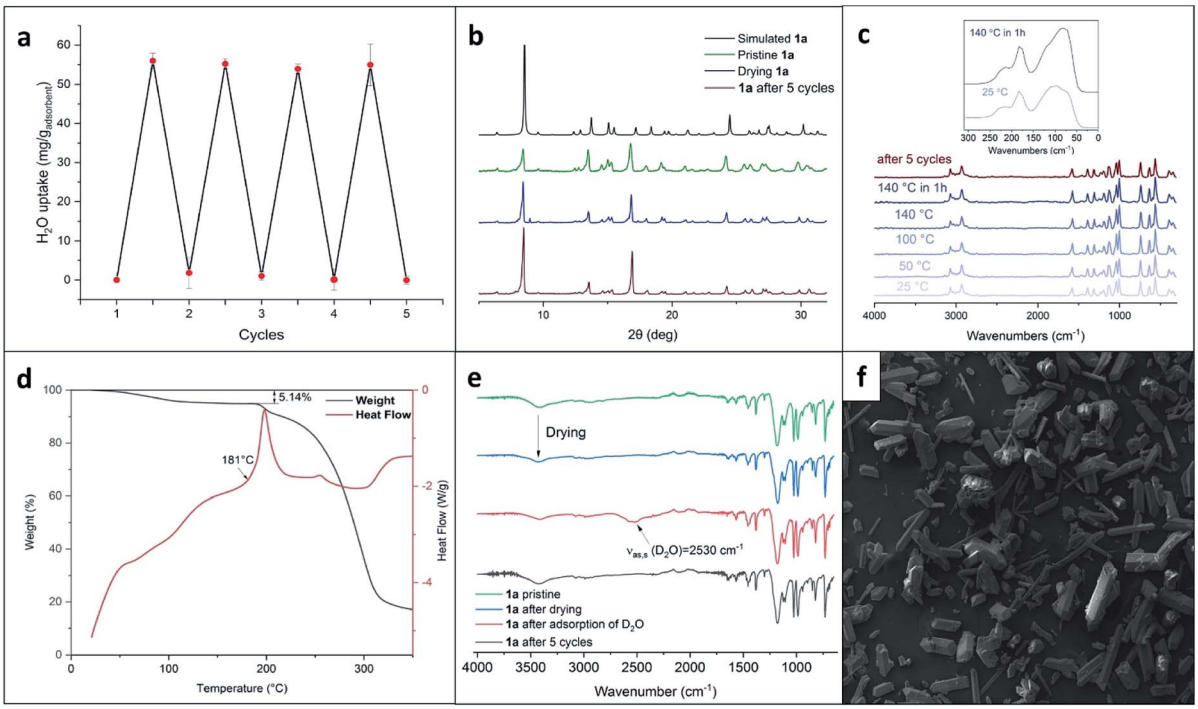

Fig. 3 (a) Repeated adsorption–desorption of water; (b) powder XRD patterns of **1a**; (c) Raman spectra of **1a** at various temperatures; (d) TG/DSC curves for **1a**; (e) FTIR spectra of **1a**; (f) SEM image of crystals of **1a**.

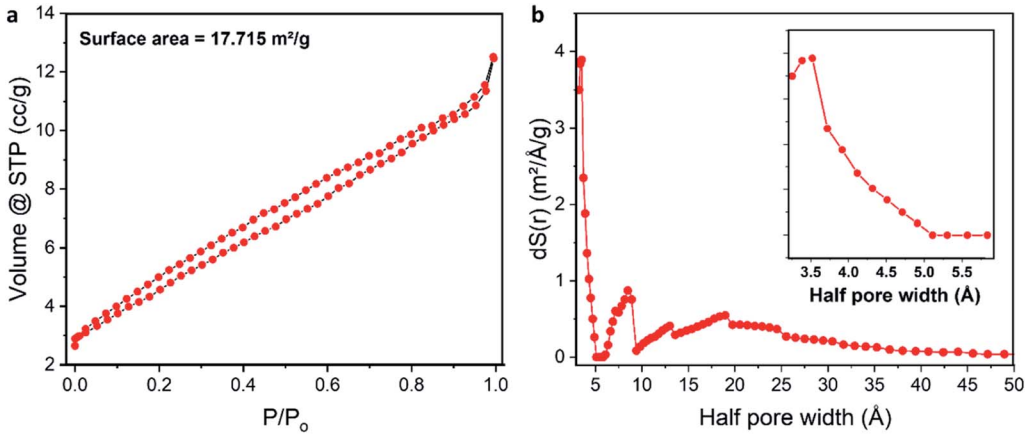

Fig. 4 (a) Nitrogen adsorption–desorption isotherm of the XOF; (b) pore size distribution curve obtained by the NLDFT approach (the enlarged image in the range from 3 to 6 Å is shown as an inset).

a diameter of approx. 10 Å; the latter value matches well with our X-ray crystallography data (Fig. 2). Other additional pores (approx. 1.7 nm) were also observed and they correspond to inter-crystallite spaces.

In the context of the discovery of the stable 3D XOF, it is noteworthy that Uriel and coworkers[31] have also employed a heterotopic tecton (featuring two σ-hole donating iodine centers, which are perpendicular to two XB accepting N sites in the same *neutral* molecule) for the design of XB-based XOFs. The assembly of this tecton led to porous XOFs with empty volumes of 20–24%. The obtained architectures were quite unstable and they irreversibly collapsed even on keeping in air at RT. This instability is believed to be associated[31] with the weakness of the XBs involved in the construction of these XOFs. In our study, we generated XOFs of a higher stability and, moreover, we demonstrated the reversibility of water adsorption–desorption associated with these materials. Most likely, the stability is determined by a stronger XB formed between *ionic sites* of our iodonium zwitterions.

Theoretical study

First, the molecular electrostatic potential (MEP) surfaces of compounds **1–3** were computed to study the degree of anisotropic distribution of the electron density around the iodine

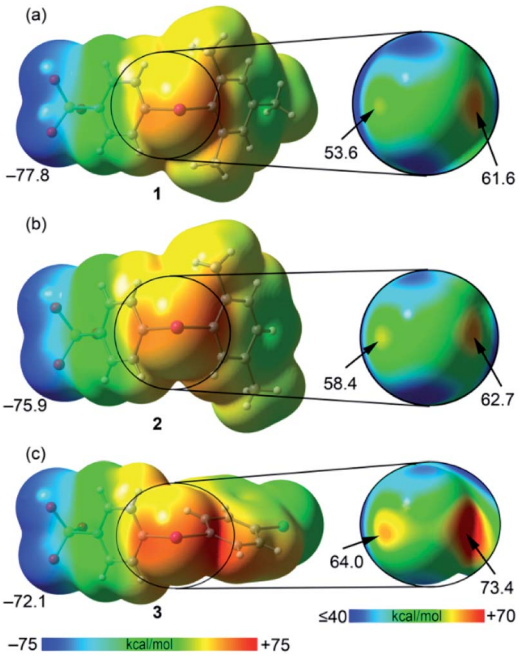

Fig. 5 MEP surfaces (0.001 au) of compounds **1** (a), **2** (b), and **3** (c), using red color for positive values and blue for negative ones. The MEP values at selected points of the surfaces are given in kcal mol^{-1}.

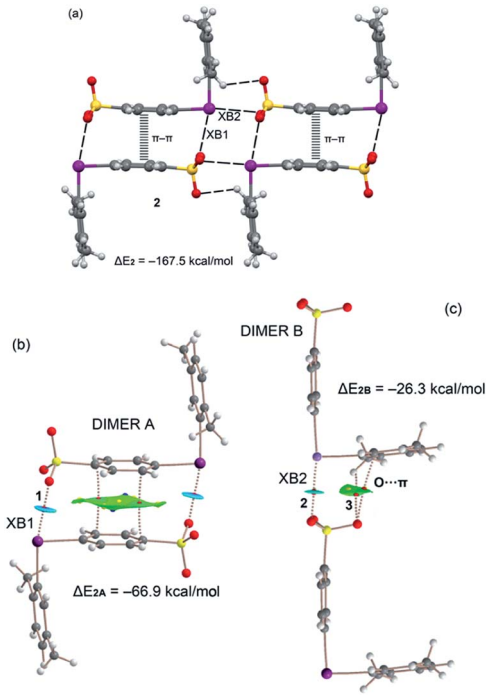

Fig. 6 (a) Tetrameric assembly present in the XRD structure of **2** thanks to an interesting combination of XBs, HBs and π–π interactions. Combined QTAIM (bond CP in red, ring CP in yellow and cage CP in blue) and NCIplot (isosurface 0.45 au, gradient cut-off 0.04 au, color range $-0.03 < \text{sign}(\lambda_2)\rho < 0.03$) of dimers A (b) and B (c); only intermolecular interactions are presented.

atom and the MEP energy difference between the two expected σ-holes (Fig. 5). As expected, the MEP values in the three compounds are positive at the iodine atom and negative at the sulfonate group. The MEP minimum is located at the O atoms of the SO_3^- group with values that range from −77.8 to −72.1 kcal mol^{-1}. The positive MEP embraces the whole iodine atoms, suggesting that the XBs involving these zwitterionic iodonium species can remain attractive even with major deviation from linearity. Nevertheless, the MEP distribution around the iodine atom is anisotropic and two σ-holes (regions of most positive electrostatic potential) are present opposite the two arene rings (Fig. 6, right panel). This indicates that more linear XBs are favored also because they are more stabilizing from the electrostatic point of view. In all cases, the σ-hole opposite the benzenesulfonate is more positive than that opposite the other arene ring. The MEP values at both σ-holes increase on going from **1** to **3**, in line with the number and electron donating/withdrawing nature of the substituents on the arene ring. In the case of compound **3**, the particularly positive MEP value at the σ-hole opposite the benzenesulfonate is partially due to the proximity of the aromatic proton.

We have also analyzed the energetic features of some supramolecular motifs observed in the prepared systems. Crystals **1b**, **2**, and **3** present very similar tetrameric and dimeric motifs which are presented in Fig. S4, 6 and S5,† respectively. The tetrameric arrays are assembled *via* XBs, HBs, and π–π interactions and their formation energies are very large, ranging from ∼−156 to ∼−184 kcal mol^{-1} (Table 2). The largest value is for compound **3** in agreement with its more positive σ-holes evidenced by the MEP surface computation. Two distinct dimeric motifs can be extracted from the tetramers present in

Table 2 Formation energies of tetramers ($\Delta E_{\text{tetramer}}$), dimers A ($\Delta E_{\text{dimer A}}$) and dimers B ($\Delta E_{\text{dimer B}}$) in compounds **1b**, **2** and **3**

Compound	$\Delta E_{\text{tetramer}}$	$\Delta E_{\text{dimer A}}$	$\Delta E_{\text{dimer B}}$
1b	−155.7	−61.2	−25.8
2	−167.5	−66.9	−26.3
3	−183.9	−74.7	−28.2

1b, **2**, and **3** and they are denoted here as dimer A and dimer B. In all three crystals, dimers A are assembled *via* two XBs and one π-stacking interaction (Fig. S4b, 6b, and S5b†). This π-stacking is expected to be highly stabilizing since the iodonium benzenesulfonate moiety is very polarized and probably its antiparallel pairing is highly exoenergetic. Indeed, the dimerization energies computed for dimers A range from ∼−61 to ∼−75 kcal mol^{-1} (Table 2). The combined QTAIM/NCIplot analysis reveals that the two equivalent XBs assembling dimers A (denoted as XB1) are characterized by a bond critical point (CP, red sphere of bond CP#1) and a bond path interconnecting the I and O atoms. Moreover, a blue NCIplot isosurface is located between the O and I atoms, thus showing a strong interaction. The π–π stacking is characterized by an extended and green isosurface that embraces both aromatic systems. The formation of dimers B is sustained by one single XB (denoted as XB2 and resulting in bond CP#2; Fig. S4c, 6c, and S5c†) and some ancillary contacts like C–H···O HBs

(resulting in bond CP#3) and O···π interactions. It is thus no surprise that the corresponding dimerization energies are significantly smaller (in absolute value) than those of dimer A (*e.g.*, −26.3 *vs.* −66.9 kcal mol^{-1} for compound **2**, Table 2). Each interaction is characterized also by the corresponding bond path and NCIplot isosurface. The blue color of the NCIplot isosurface that characterizes XB2 is less intense than that of XB1, thus suggesting that XB1 is stronger, in line with the shorter XB experimental distance (Table 1).

As described above, the solid-state architecture of compound **1a** is different from that of **1b**, **2**, and **3** and the tetrameric motif observed in these three latter crystals is not present in **1a**, while the two dimeric motifs A and B are present with minor differences in the interaction pattern with respect to **1b**, **2**, and **3** (Fig. 7). QTAIM/NCIplot analysis reveals that dimer A in **1a** is assembled *via* two XBs (denoted as XB1) and one π-stacking, while dimer B is assembled *via* one single XB (denoted as XB2) and a weak ancillary C–H···O HB between one methyl group and one O atom of the sulfonate group. Consistent with these interaction patterns, the stabilization energy of dimer A (−62.3 kcal mol^{-1}) is much greater than that of dimer B (−28.1 kcal mol^{-1}).

Finally, taking into consideration that the σ-hole opposite the benzenesulfonate group is more positive than the other one, the fact that XB1 is shorter and stronger than XB2 can probably be explained considering the favorable interplay between the π-stacking and the XBs in dimers A. That is, the co-existing π-stacking and XB interactions reinforce each other.

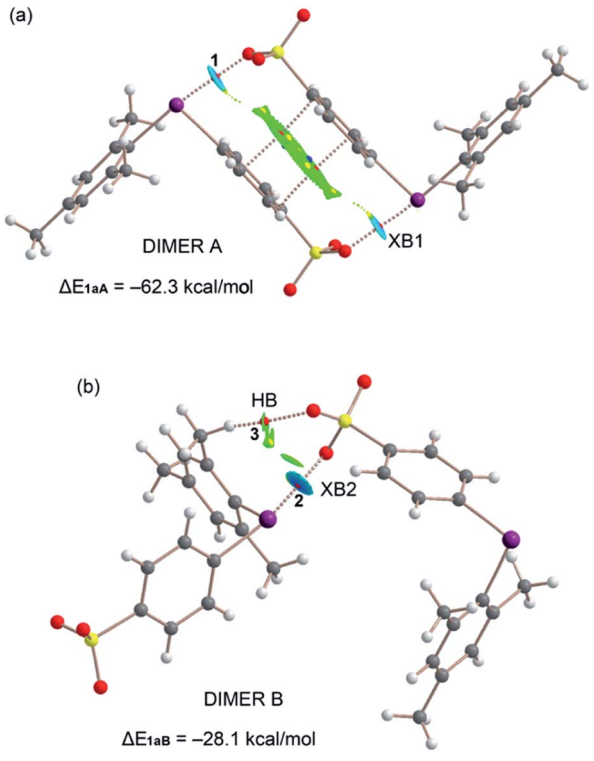

Fig. 7 Combined QTAIM (bond CP in red, ring CP in yellow and cage CP in blue) and NCIplot (isosurface 0.45 au, gradient cut-off 0.04 au, color range −0.03 < sign(λ_2)ρ < 0.03) of dimers A (a) and B (b); only intermolecular interactions are shown.

Conclusion

The results reported in this paper prove that the high directionality of XB makes this interaction suitable for the formation of XOFs if the involved tectons are able to translate this interaction feature into a crystal architecture feature. With the aim of preparing the first one-component 3D XOFs, we focused our attention on zwitterionic aryliodonium tectons on the assumption that the geometrical constraints resulting from the tendency of the hypervalent iodine atoms of these derivatives to act as bidentate XB donors might favor XOF formation *vs.* interpenetration. Thanks to the electrostatic attraction between the cationic XB donor and the anionic XB acceptor, these hypervalent iodine atoms tend to form remarkably strong XBs thus enabling the formation of XOFs robust enough to survive when the water occupying the channels is almost quantitatively removed and readsorbed.

Specifically, the single crystal X-ray analyses of **1a** and **1b**, the two polymorphic crystals formed by one of the zwitterionic 4-(aryliodonium)benzenesulfonates described here, reveal the presence of porous architectures wherein parallel channels are arranged in honeycomb and rectangular patterns, respectively. These two polymorphs are the first cases of one-component 3D XOFs reported up to now. The diameter of the channels spans the range 1.0–1.2 nanometers and the percentage of empty volume varies from 22.5 to 25.0. The powder X-ray analysis shows that no change of the crystalline architecture occurs when the solvent is removed from the cavities or when it refills the emptied cavities. Computation of MEP surfaces of the zwitterions confirms the relevance of the iodine σ-holes in determining the charge assisted XBs driving the formation of the observed architectures, and QTAIM/NCIplot analyses prove the robustness of these interactions. Importantly, while the porosity of **1a** and **1b** is not particularly high, the relevance of the obtainment of these systems consists in the fact that their crystalline architectures afford a proof of concept for the potential of zwitterionic aryliodonium tectons in affording robust one-component 3D XOFs. Greater porosity might be obtained by modifying the structure of the used zwitterionic aryliodonium tectons, *e.g.*, by employing zwitterions with an increased separation between the anionic and cationic sites.

Data availability

Crystallographic data for **1–3** has been deposited at the Cambridge Crystallographic Data Centre under CCDC 2096180, 2096183, 2096184 and 2096193 and can be obtained from **https://www.ccdc.cam.ac.uk/data request/cif**. The associated data are available from the authors upon reasonable request.

Author contributions

N. S. S. and O. S. K. – investigation; P. S. P., D. M. I., M. S. Yu. and R. M. G. – data curation; D. M. I. and M. S. Yu. – formal

analysis; P. S. P., T. W., V. V. Zh., A. F. and V. Yu. K. – project administration; N. S. S., A. F. and V. Yu. K. – writing the original draft; P. S. P., T. W., V. V. Zh. and G. R. – proofreading of the original draft; N. S. S. and G. R. – funding acquisition.

Conflicts of interest

There are no conflicts to declare.

Acknowledgements

This work was funded by the Russian Science Foundation grant 21-73-00148 (Synthetic part and studies of physicochemical properties of XOFs) and the Ministry of Science and Higher Education of the Russian Federation in the framework of the "Mega-grant" project (No. 075-15-2021-585; crystal engineering). The authors are grateful to the Center for X-ray Diffraction Studies, Magnetic Resonance Research Center, and Center for Chemical Analysis and Materials Research (Saint Petersburg State University) and the Tomsk Regional Core Shared Research Facilities Centre (National Research Tomsk State University) for the physicochemical studies. The TG/DSC study was carried out using the core facilities of "Physical and Chemical Methods of Analysis" (National Research Tomsk Polytechnic University). O. G. and Y. Y. are also grateful to the JST-ERATO Yamauchi Materials Space-Tectonics Project (JPMJER2003). This work was performed in part at the Queensland node of the Australian National Fabrication Facility, a company established under the National Collaborative Research Infrastructure Strategy to provide nano and microfabrication facilities for Australia's researchers.

References

1 H. Li, L. Li, R.-B. Lin, W. Zhou, Z. Zhang, S. Xiang and B. Chen, *EnergyChem*, 2019, **1**, 100006.
2 Á. Berenguer-Murcia, J. P. Marco-Lozar and D. Cazorla-Amorós, *Chem. Rec.*, 2018, **18**, 900–912.
3 D. Banerjee, C. M. Simon, S. K. Elsaidi, M. Haranczyk and P. K. Thallapally, *Chem*, 2018, **4**, 466–494.
4 X. Zou and G. Zhu, *Adv. Mater.*, 2018, **30**, 1700750.
5 O. Guselnikova, Y. Kalachyova, R. Elashnikov, M. Cieslar, Z. Kolska, P. Sajdl, P. Postnikov, V. Svorcik and O. Lyutakov, *Microporous Mesoporous Mater.*, 2020, **309**, 110577.
6 Y. Wang, H. Jin, Q. Ma, K. Mo, H. Mao, A. Feldhoff, X. Cao, Y. Li, F. Pan and Z. Jiang, *Angew. Chem., Int. Ed.*, 2020, **59**, 4365–4369.
7 S. Feng, Y. Shang, Z. Wang, Z. Kang, R. Wang, J. Jiang, L. Fan, W. Fan, Z. Liu, G. Kong, Y. Feng, S. Hu, H. Guo and D. Sun, *Angew. Chem., Int. Ed.*, 2020, **59**, 3840–3845.
8 L. Zhu, D. Shen and K. H. Luo, *J. Hazard. Mater.*, 2020, **389**, 122102.
9 T. Islamoglu, Z. Chen, M. C. Wasson, C. T. Buru, K. O. Kirlikovali, U. Afrin, M. R. Mian and O. K. Farha, *Chem. Rev.*, 2020, **120**, 8130–8160.
10 N. Zhang, A. Ishag, Y. Li, H. Wang, H. Guo, P. Mei, Q. Meng and Y. Sun, *J. Cleaner Prod.*, 2020, **277**, 123360.
11 S. Sudan, A. Gładysiak, B. Valizadeh, J.-H. Lee and K. C. Stylianou, *Inorg. Chem.*, 2020, **59**, 9029–9036.
12 D. A. Anito, T.-X. Wang, Z.-W. Liu, X. Ding and B.-H. Han, *J. Hazard. Mater.*, 2020, **400**, 123188.
13 X. Fan and Y. Jiao, in *Sustainable Nanoscale Engineering*, Elsevier, 2020, pp. 115–137.
14 T. A. Goetjen, J. Liu, Y. Wu, J. Sui, X. Zhang, J. T. Hupp and O. K. Farha, *Chem. Commun.*, 2020, **56**, 10409–10418.
15 F. Jin, J. Liu, Y. Chen and Z. Zhang, *Angew. Chem., Int. Ed.*, 2021, **60**, 14222–14235.
16 F. N. Al-Rowaili, A. Jamal, M. S. Ba Shammakh and A. Rana, *ACS Sustainable Chem. Eng.*, 2018, **6**, 15895–15914.
17 O. Guselnikova, A. Trelin, E. Miliutina, R. Elashnikov, P. Sajdl, P. Postnikov, Z. Kolska, V. Svorcik and O. Lyutakov, *ACS Appl. Mater. Interfaces*, 2020, **12**, 28110–28119.
18 W. Yang, A. Greenaway, X. Lin, R. Matsuda, A. J. Blake, C. Wilson, W. Lewis, P. Hubberstey, S. Kitagawa, N. R. Champness and M. Schröder, *J. Am. Chem. Soc.*, 2010, **132**, 14457–14469.
19 J. Lü, C. Perez-Krap, M. Suyetin, N. H. Alsmail, Y. Yan, S. Yang, W. Lewis, E. Bichoutskaia, C. C. Tang, A. J. Blake, R. Cao and M. Schröder, *J. Am. Chem. Soc.*, 2014, **136**, 12828–12831.
20 K.-D. Zhang, J. Tian, D. Hanifi, Y. Zhang, A. C.-H. Sue, T.-Y. Zhou, L. Zhang, X. Zhao, Y. Liu and Z.-T. Li, *J. Am. Chem. Soc.*, 2013, **135**, 17913–17918.
21 J. Luo, J.-W. Wang, J.-H. Zhang, S. Lai and D.-C. Zhong, *CrystEngComm*, 2018, **20**, 5884–5898.
22 B. Wang, R.-B. Lin, Z. Zhang, S. Xiang and B. Chen, *J. Am. Chem. Soc.*, 2020, **142**, 14399–14416.
23 P. Li, M. R. Ryder and J. F. Stoddart, *Acc. Mater. Res.*, 2020, **1**, 77–87.
24 T. Adachi and M. D. Ward, *Acc. Chem. Res.*, 2016, **49**, 2669–2679.
25 A. Pulido, L. Chen, T. Kaczorowski, D. Holden, M. A. Little, S. Y. Chong, B. J. Slater, D. P. McMahon, B. Bonillo, C. J. Stackhouse, A. Stephenson, C. M. Kane, R. Clowes, T. Hasell, A. I. Cooper and G. M. Day, *Nature*, 2017, **543**, 657–664.
26 I. Hisaki, C. Xin, K. Takahashi and T. Nakamura, *Angew. Chem., Int. Ed.*, 2019, **58**, 11160–11170.
27 J. Lü and R. Cao, *Angew. Chem., Int. Ed.*, 2016, **55**, 9474–9480.
28 M. A. Little and A. I. Cooper, *Adv. Funct. Mater.*, 2020, **30**, 1909842.
29 S. Shankar, O. Chovnik, L. J. W. Shimon, M. Lahav and M. E. van der Boom, *Cryst. Growth Des.*, 2018, **18**, 1967–1977.
30 N. Chongboriboon, K. Samakun, T. Inprasit, F. Kielar, W. Dungkaew, L. W.-Y. Wong, H. H.-Y. Sung, D. B. Ninković, S. D. Zarić and K. Chainok, *CrystEngComm*, 2020, **22**, 24–34.
31 L. González, S. Graus, R. M. Tejedor, P. López, J. Elguero, J. L. Serrano and S. Uriel, *CrystEngComm*, 2018, **20**, 3167–3170.

32 P. Metrangolo, F. Meyer, T. Pilati, G. Resnati and G. Terraneo, *Angew. Chem., Int. Ed.*, 2008, **47**, 6114–6127.
33 C. B. Aakeröy and C. L. Spartz, in *Halogen Bonding I*, Springer, 2014, pp. 155–182.
34 S. v. Lindeman, J. Hecht and J. K. Kochi, *J. Am. Chem. Soc.*, 2003, **125**, 11597–11606.
35 P. Metrangolo, F. Meyer, T. Pilati, D. M. Proserpio and G. Resnati, *Chem.–Eur. J.*, 2007, **13**, 5765–5772.
36 R. Thaimattam, C. V. K. Sharma, A. Clearfield and G. R. Desiraju, *Cryst. Growth Des.*, 2001, **1**, 103–106.
37 C. A. Gunawardana, M. Đaković and C. B. Aakeröy, *Chem. Commun.*, 2018, **54**, 607–610.
38 S. M. Oburn, C. L. Santana, E. Elacqua and R. H. Groeneman, *CrystEngComm*, 2020, **22**, 4349–4352.
39 G. Gong, S. Lv, J. Han, F. Xie, Q. Li, N. Xia, W. Zeng, Y. Chen, L. Wang, J. Wang and S. Chen, *Angew. Chem.*, 2021, **133**, 14957–14961.
40 R. B. Walsh, C. W. Padgett, P. Metrangolo, G. Resnati, T. W. Hanks and W. T. Pennington, *Cryst. Growth Des.*, 2001, **1**, 165–175.
41 G. Marras, P. Metrangolo, F. Meyer, T. Pilati, G. Resnati and A. Vij, *New J. Chem.*, 2006, **30**, 1397.
42 J. Martí-Rujas, L. Colombo, J. Lü, A. Dey, G. Terraneo, P. Metrangolo, T. Pilati and G. Resnati, *Chem. Commun.*, 2012, **48**, 8207.
43 K. Raatikainen and K. Rissanen, *Chem. Sci.*, 2012, **3**, 1235.
44 M. S. Yusubov, A. V. Maskaev and V. V. Zhdankin, *Arkivoc*, 2011, **2011**, 370–409.
45 E. Merritt and B. Olofsson, *Angew. Chem., Int. Ed.*, 2009, **48**, 9052–9070.
46 L. Catalano, G. Cavallo, P. Metrangolo, G. Resnati and G. Terraneo, in *Topics in Current Chemistry*, Springer Verlag, 2016, vol. 373, pp. 289–309.
47 F. Bailly, P. Barthen, H. J. Frohn and M. Köckerling, *Z. Anorg. Allg. Chem.*, 2000, **626**, 2419–2427.
48 N. E. Zhukhlistova, G. N. Tishchenko, T. P. Tolstaya and L. D. Asulyan, *Crystallogr. Rep.*, 2001, **46**, 631–635.
49 P. S. Postnikov, O. A. Guselnikova, M. S. Yusubov, A. Yoshimura, V. N. Nemykin and V. V. Zhdankin, *J. Org. Chem.*, 2015, **80**, 5783–5788.
50 M. S. Yusubov, D. Yu. Svitich, A. Yoshimura, B. J. Kastern, V. N. Nemykin and V. V. Zhdankin, *Eur. J. Org. Chem.*, 2015, **2015**, 4831–4834.
51 G. Cavallo, J. S. Murray, P. Politzer, T. Pilati, M. Ursini and G. Resnati, *IUCrJ*, 2017, **4**, 411–419.
52 N. S. Soldatova, V. V. Suslonov, T. Yu. Kissler, D. M. Ivanov, A. S. Novikov, M. S. Yusubov, P. S. Postnikov and V. Yu. Kukushkin, *Crystals*, 2020, **10**, 230.
53 N. S. Soldatova, P. S. Postnikov, V. V. Suslonov, T. Yu. Kissler, D. M. Ivanov, M. S. Yusubov, B. Galmés, A. Frontera and V. Yu. Kukushkin, *Org. Chem. Front.*, 2020, **7**, 2230–2242.
54 F. Heinen, E. Engelage, A. Dreger, R. Weiss and S. M. Huber, *Angew. Chem., Int. Ed.*, 2018, **57**, 3830–3833.
55 F. Heinen, E. Engelage, C. J. Cramer and S. M. Huber, *J. Am. Chem. Soc.*, 2020, **142**, 8633–8640.
56 F. Heinen, D. L. Reinhard, E. Engelage and S. M. Huber, *Angew. Chem., Int. Ed.*, 2021, **60**(10), 5069–5073.
57 R. L. Sutar and S. M. Huber, *ACS Catal.*, 2019, **9**, 9622–9639.
58 C. R. Hubbard, V. L. Himes, A. D. Mighell and S. W. Page, *Acta Crystallogr., Sect. B: Struct. Crystallogr. Cryst. Chem.*, 1980, **36**, 2819–2821.
59 D. D. DesMarteau, W. T. Pennington, V. Montanari and B. H. Thomas, *J. Fluorine Chem.*, 2003, **122**, 57–61.
60 M. W. Justik, J. D. Protasiewicz and J. B. Updegraff, *Tetrahedron Lett.*, 2009, **50**, 6072–6075.
61 R. Robidas, V. Guérin, L. Provençal, M. Echeverria and C. Y. Legault, *Org. Lett.*, 2017, **19**, 6420–6423.
62 P. Caramenti, S. Nicolai and J. Waser, *Chem.–Eur. J.*, 2017, **23**, 14702–14706.
63 A. Yoshimura, M. T. Shea, O. Guselnikova, P. S. Postnikov, G. T. Rohde, A. Saito, M. S. Yusubov, V. N. Nemykin and V. V. Zhdankin, *Chem. Commun.*, 2018, **54**, 10363–10366.
64 M. S. Yusubov, R. Y. Yusubova, V. N. Nemykin and V. V. Zhdankin, *J. Org. Chem.*, 2013, **78**, 3767–3773.
65 M. S. Yusubov, N. S. Soldatova, P. S. Postnikov, R. R. Valiev, D. Y. Svitich, R. Y. Yusubova, A. Yoshimura, T. Wirth and V. V. Zhdankin, *Eur. J. Org. Chem.*, 2018, **2018**, 640–647.
66 N. Soldatova, P. Postnikov, O. Kukurina, V. V Zhdankin, A. Yoshimura, T. Wirth and M. S. Yusubov, *Beilstein J. Org. Chem.*, 2018, **14**, 849–855.
67 N. S. Antonkin, Y. A. Vlasenko, A. Yoshimura, V. I. Smirnov, T. N. Borodina, V. V. Zhdankin, M. S. Yusubov, A. Shafir and P. S. Postnikov, *J. Org. Chem.*, 2021, **86**, 7163–7178.
68 L. D. Caspers, J. Spils, M. Damrath, E. Lork and B. J. Nachtsheim, *J. Org. Chem.*, 2020, **85**, 9161–9178.
69 A. Bondi, *J. Phys. Chem.*, 1964, **68**, 441–451.
70 A. L. Spek, *PLATON, A Multipurpose Crystallographic Tool*, 2005, Utrecht University, Utrecht, The Netherlands.
71 J. Jagiello, J. Kenvin, A. Celzard and V. Fierro, *Carbon*, 2019, **144**, 206–215.